

THERMAL INSTABILITY WITH ANISOTROPIC THERMAL CONDUCTION AND ADIABATIC COSMIC RAYS: IMPLICATIONS FOR COLD FILAMENTS IN GALAXY CLUSTERS

PRATEEK SHARMA¹, IAN J. PARRISH¹, AND ELIOT QUATAERT

Astronomy Department and Theoretical Astrophysics Center, University of California, Berkeley, CA 94720, USA; psharma@astro.berkeley.edu,
iparrish@astro.berkeley.edu, eliot@astro.berkeley.edu

Received 2010 March 20; accepted 2010 July 7; published 2010 August 12

ABSTRACT

Observations of the cores of nearby galaxy clusters show H α and molecular emission-line filaments. We argue that these are the result of *local* thermal instability in a *globally* stable galaxy cluster core. We present local, high-resolution, two-dimensional magnetohydrodynamic simulations of thermal instability for conditions appropriate to the intracluster medium (ICM); the simulations include anisotropic thermal conduction along magnetic field lines and adiabatic cosmic rays. Thermal conduction suppresses thermal instability along magnetic field lines on scales smaller than the Field length ($\gtrsim 10$ kpc for the hot, diffuse ICM). We show that the Field length in the cold medium must be resolved both along and perpendicular to the magnetic field in order to obtain numerically converged results. Because of negligible conduction perpendicular to the magnetic field, thermal instability leads to fine scale structure in the perpendicular direction. Filaments of cold gas along magnetic field lines are thus a natural consequence of thermal instability with anisotropic thermal conduction. This is true even in the fully nonlinear regime and even for dynamically weak magnetic fields. The filamentary structure in the cold gas is also imprinted on the diffuse X-ray-emitting plasma in the neighboring hot ICM. Nonlinearly, filaments of cold ($\sim 10^4$ K) gas should have lengths (along the magnetic field) comparable to the Field length in the cold medium $\sim 10^{-4}$ pc! Observations show, however, that the atomic filaments in clusters are far more extended, ~ 10 kpc. Cosmic-ray pressure support (or a small-scale turbulent magnetic pressure) may resolve this discrepancy: even a small cosmic-ray pressure in the diffuse ICM, $\sim 10^{-4}$ of the thermal pressure, can be adiabatically compressed to provide significant pressure support in cold filaments. This is qualitatively consistent with the large population of cosmic rays invoked to explain the atomic and molecular line ratios observed in filaments.

Key words: conduction – galaxies: clusters: intracluster medium – instabilities – magnetic fields

Online-only material: color figures

1. INTRODUCTION

The thermal instability has been studied extensively in the context of the interstellar medium (ISM; Field 1965; Koyama & Inutsuka 2000; Sánchez-Salcedo et al. 2002; Kritsuk & Norman 2002; Piontek & Ostriker 2004; Audit & Hennebelle 2005) and the formation of solar prominences (e.g., Karpen et al. 1988), but its role in galaxy clusters has not received as much attention. The cooling time in the intracluster medium (ICM) near the centers of galaxy clusters may be as short as 10–100 Myr. Observations show that there is a dramatic *lack* of plasma below ~ 1 keV (e.g., Peterson et al. 2003), inconsistent with the prediction of the original cooling flow models (e.g., Fabian 1994). In addition, the star formation rate in the central galaxy is 10–100 times smaller than if the gas cooled at the predicted rate (e.g., O’Dea et al. 2008). This implies that cooling in the ICM is balanced by some form of heating that maintains an approximate global thermal equilibrium. Feedback from a central active galactic nucleus (AGN) is an energetically plausible source of the required heating (e.g., Guo et al. 2008). However, precisely how the AGN provides this heating is not understood in detail; nor are other heating mechanisms ruled out. Many clusters with a short central cooling time ($\lesssim 1$ Gyr; or equivalently a low central entropy) show both star formation and H α emission, indicative of cool plasma at $\lesssim 10^4$ K (e.g., Cavagnolo et al. 2008). Even if heating balances cooling in a global sense, the ICM plasma is expected to be *locally* thermally unstable because of the form of the cooling function (e.g., Field 1965). This local thermal

instability is an attractive mechanism for producing the H α and molecular filaments seen in clusters with short cooling times.

Recently, the atomic and molecular filaments in the core of the Perseus cluster have been spatially resolved (e.g., Conselice et al. 2001; Salomé et al. 2006). Based on the narrowness and coherence of these filaments, Fabian et al. (2008) suggested that magnetic fields play a critical role in the dynamics of the filaments. In addition to the possible role of magnetic pressure and tension, the magnetic field also modifies the microscopic transport processes in the ICM because the mean free path along magnetic field lines is orders of magnitude larger than the gyroradius. As a result, thermal conduction is primarily along magnetic field lines (Braginskii 1965).

This paper centers on carrying out magnetohydrodynamic (MHD) simulations of thermal instability with thermal conduction along magnetic field lines. We focus on understanding the physics of the thermal instability in the ICM, rather than on making detailed comparisons with observations. Throughout this paper we ignore the possible presence of a background gravitational field. This allows us to study the physics of the thermal instability without the added complication of buoyant motions, inflow, etc. In addition to including the effects of anisotropic heat transport, we also include cosmic rays as a second fluid. Even an initially small cosmic-ray pressure can become energetically important in cold filaments. Part of the motivation for including cosmic rays is that a significant population of energetic ions ($\gg eV$, the temperature of optical filaments) appear required to explain the observed line ratios in filaments in galaxy clusters (Ferland et al. 2009).

¹ Chandra/Einstein Fellow.

The multiphase nature of the ICM is physically analogous to the well-studied multiphase ISM. The ISM has three dominant phases: a molecular phase at ~ 100 K, an atomic phase at $\sim 10^4$ K, and the hot phase at 10^6 K. The cooling function in the ISM is thermally bistable with thermally stable phases at ~ 100 K and $\sim 10^4$ K. The hot phase is thermally unstable but is probably maintained at its temperature by supernova heating (McKee & Ostriker 1977). The same physical considerations apply for the ICM, except that the hot phase is maintained by a still poorly understood heating process (e.g., AGN feedback).

This paper is organized as follows. Section 2 summarizes our model equations and the results of a linear stability analysis including conduction along field lines, cosmic rays, and magnetic fields (see the Appendix). Section 3 presents the numerical set-up and the results of our numerical simulations. Section 4 discusses the astrophysical implications of our results.

2. GOVERNING EQUATIONS AND NUMERICAL METHODS

A magnetized plasma with cosmic rays can be described by the following two-fluid equations:

$$\frac{d\rho}{dt} = -\rho \nabla \cdot \mathbf{v}, \quad (1)$$

$$\rho \frac{d\mathbf{v}}{dt} = -\nabla \left(p + p_{\text{cr}} + \frac{B^2}{8\pi} \right) + \frac{(\mathbf{B} \cdot \nabla) \mathbf{B}}{4\pi}, \quad (2)$$

$$\frac{\partial \mathbf{B}}{\partial t} = \nabla \times (\mathbf{v} \times \mathbf{B}), \quad (3)$$

$$\frac{de}{dt} - \frac{\gamma e}{\rho} \frac{d\rho}{dt} = -n_e n_i \Lambda(T) - \nabla \cdot \mathbf{Q} + H(t), \quad (4)$$

and

$$\frac{dp_{\text{cr}}}{dt} - \frac{\gamma_{\text{cr}} p_{\text{cr}}}{\rho} \frac{d\rho}{dt} = -\nabla \cdot \boldsymbol{\Gamma}, \quad (5)$$

where $d/dt = \partial/\partial t + \mathbf{v} \cdot \nabla$ is the Lagrangian time derivative, $\Lambda(T)$ is the cooling function,

$$\mathbf{Q} = -\kappa_{\parallel} \hat{\mathbf{b}} (\hat{\mathbf{b}} \cdot \nabla) T \quad (6)$$

is the heat flux along magnetic field lines,

$$\boldsymbol{\Gamma} = -D_{\parallel} \hat{\mathbf{b}} (\hat{\mathbf{b}} \cdot \nabla) p_{\text{cr}} \quad (7)$$

is the diffusive cosmic-ray energy flux (multiplied by $[\gamma_{\text{cr}} - 1]$), ρ is the mass density, n_e and n_i are the electron and ion number densities respectively, \mathbf{v} is the common bulk-flow velocity of the thermal plasma and cosmic rays, \mathbf{B} is the magnetic field, $\hat{\mathbf{b}} = \mathbf{B}/B$, p and p_{cr} are the thermal-plasma and cosmic-ray pressures, κ_{\parallel} is the parallel thermal conductivity, D_{\parallel} is the diffusion coefficient for cosmic-ray transport along the magnetic field, and $\gamma = 5/3$ and $\gamma_{\text{cr}} = 4/3$ are the adiabatic indices of the thermal plasma and cosmic rays, respectively. We assume one-third solar metallicity so that the mean molecular weights are $\mu = 0.62$ and $\mu_e = 1.18$. We do not include gravity in the momentum equation (Equation (2)) in order to focus on the thermal physics. Note that our model equations also do not include the streaming of cosmic rays relative to the thermal plasma, which provides a mechanism for heating the thermal plasma (e.g., Loewenstein et al. 1991; Guo & Oh 2008). This is

numerically subtle to include (Sharma et al. 2009c) and will be studied in future work.

It is difficult to study the problem of thermal instability without a well-defined equilibrium state. In order to ensure that we have such a state, at each time step the heating term $H(t)$ in Equation (4) is updated so that the volume-averaged heating and cooling in our computational domain balance each other. Without such heating, the plasma as a whole cools to very low temperatures on a cooling time (the same timescale on which the thermal instability is developing). Since the source of heating and its functional form are not that well understood in the ICM, we choose a constant heating per unit volume for simplicity. Calculations with a constant heating per unit mass, i.e., $H(t) \propto \rho$, yield very similar results because cooling ($\propto n^2$) dominates in the cold phase and heating dominates in the hot phase in both cases.

2.1. Linear Stability

In the Appendix we study the linear thermal stability of a uniform plasma with magnetic fields, cosmic rays, and thermal conduction along magnetic field lines. To isolate the physics of interest in this paper, we focus on the “condensation mode,” i.e., the entropy mode. This calculation is a straightforward generalization of previous results (e.g., Field 1965), but we include it for completeness. Here we quote the final results.

When the cosmic-ray and magnetic pressures are negligible compared to the plasma pressure, and the cooling time t_{cool} is long compared to the sound-crossing time, the growth rate for the thermal instability (σ) is given by

$$\sigma \gamma = -\chi_{\parallel} k_{\parallel}^2 - t_{\text{cool}}^{-1} \frac{d \ln(\Lambda/T^2)}{d \ln T}, \quad (8)$$

where $t_{\text{cool}}^{-1} \equiv (\gamma - 1) n_e n_i \Lambda / p$. Note that the thermal conductivity, κ_{\parallel} , in Equation (6) is related to the diffusivity used here, χ_{\parallel} , by $\kappa_{\parallel} = n_e k_B \chi_{\parallel}$. The first term on the right-hand side of Equation (8) describes the conductive stabilization of modes with short wavelengths parallel to the local magnetic field (large k_{\parallel}). This implies that the fastest growing modes will be elongated along the magnetic field lines and hence filamentary. The critical parallel length scale at which $\sigma = 0$ (the Field length) is given by

$$\lambda_F \equiv 2\pi \left[\frac{\chi_{\parallel} t_{\text{cool}}}{d \ln(T^2/\Lambda)/d \ln T} \right]^{1/2}. \quad (9)$$

When the cosmic-ray and/or magnetic pressure is large compared to the plasma pressure, the isochoric growth rate applies, i.e.,

$$\sigma = -\chi_{\parallel} k_{\parallel}^2 - t_{\text{cool}}^{-1} \frac{d \ln \Lambda}{d \ln T}. \quad (10)$$

This is also applicable when the cooling time is shorter than the sound-crossing time, irrespective of the magnetic and cosmic-ray contributions to the total pressure. However, for typical ICM conditions, the cooling time in the hot plasma is longer than the sound-crossing time.

2.2. Thermal Conductivity and the Cooling Function

The thermal conductivity of a fully ionized plasma is governed by electron collisions with the background ions and electrons. We are interested in plasmas hotter than 10^4 K, so that

$$\kappa_{\parallel} = \frac{1.84 \times 10^{-5}}{\ln \lambda} T^{5/2} \text{erg s}^{-1} \text{K}^{-7/2} \text{cm}^{-1}, \quad (11)$$

where we use a Coulomb logarithm of $\ln \lambda = 37$. Since the Larmor radius of electrons is much smaller than their collisional mean free path, thermal conduction is only effective along magnetic field lines; the perpendicular transport is negligible.

We use the cooling function for an ionized plasma from Sutherland & Dopita (1993). A fit to the Sutherland and Dopita cooling rates for a third solar metallicity is given by (a generalization of Tozzi & Norman 2001):

$$\begin{aligned} \Lambda &= 10^{-22} (8.6 \times 10^{-3} T_{\text{keV}}^{-1.7} + 0.058 T_{\text{keV}}^{0.5} + 0.063) \text{ erg s}^{-1} \text{ cm}^3 \\ &\quad \text{for } T > 0.02 \text{ keV}, \\ \Lambda &= 6.72 \times 10^{-22} (T_{\text{keV}}/0.02)^{0.6} \text{ erg s}^{-1} \text{ cm}^3 \\ &\quad \text{for } T \leq 0.02 \text{ keV}, T \geq 0.0017235 \text{ keV}, \\ \Lambda &= 1.544 \times 10^{-22} (T_{\text{keV}}/0.0017235)^6 \text{ erg s}^{-1} \text{ cm}^3 \\ &\quad \text{for } T < 0.0017235 \text{ keV}, \end{aligned} \quad (12)$$

where T_{keV} is the temperature in keV. For the cooling function given by Equation (12), the only phase that is thermally stable according to Equation (8) is plasma with $T \lesssim 0.0017 \text{ keV} \simeq 10^4 \text{ K}$.

Koyama & Inutsuka (2004) have shown that with isotropic conduction, thermal instability simulations do not converge with increasing resolution unless the Field length is always resolved by a few grid cells. We find the same result in our simulations. The Field length can be written as

$$\lambda_F \approx 14.4 T_{\text{keV}}^{7/4} (n_{e,0.1} n_{i,0.1})^{-1/2} \Lambda_{-23}^{-1/2} \left[\frac{d \ln(T^2/\Lambda)}{d \ln T} \right]^{-1/2} \text{ kpc}, \quad (13)$$

where $n_{e,0.1}$ ($n_{i,0.1}$) is the electron (ion) number density in units of 0.1 cm^{-3} and $\Lambda = 10^{-23} \Lambda_{-23} \text{ erg s}^{-1} \text{ cm}^3$. Because the Field length decreases rapidly with decreasing temperature, it is prohibitive to resolve the Field length in a numerical simulation if the plasma has a wide range of temperatures. Indeed, at a fixed pressure, Equation (13) implies that the Field length at a few 10^4 K is $\approx 10^8$ times smaller than at 1 keV! In order to ensure that our simulations always resolve the properties of the cold phase of the ICM, we use an artificial cooling function in which the thermally stable phase is at a much higher temperature of $2 \times 10^6 \text{ K}$. Because our simulations begin with plasma at typical ICM temperatures $\sim 10^7 \text{ K}$, the modest range of temperatures on the computational domain makes it feasible to always resolve the Field length. Figure 1 shows a comparison of the true cooling function from Equation (12) (solid line) and our modified cooling function (dotted line).

With anisotropic thermal conduction, we find that numerical convergence requires resolving both the parallel and perpendicular Field lengths in the cold stable phase. More precisely, if the perpendicular Field length is not resolved, the width of cold structures perpendicular to the local magnetic field decreases with increasing resolution. In order to ensure that there are no spurious results due to unresolved structures at the grid scale, we thus include a constant *isotropic* diffusivity of $3 \times 10^{26} \text{ cm}^2 \text{ s}^{-1}$, in addition to the parallel thermal conductivity given by Equation (11). The perpendicular diffusivity required for numerical convergence depends on resolution; we have verified numerically that $\approx 3 \times 10^{26} \text{ cm}^2 \text{ s}^{-1}$ is the minimum isotropic diffusivity required to obtain converged results for our two-dimensional simulations presented in Section 4. The thermal diffusivity along magnetic field lines (Equation (11)) is ≈ 30 times larger than the isotropic diffusivity for our typical initial conditions. Thus thermal conduction is still primarily

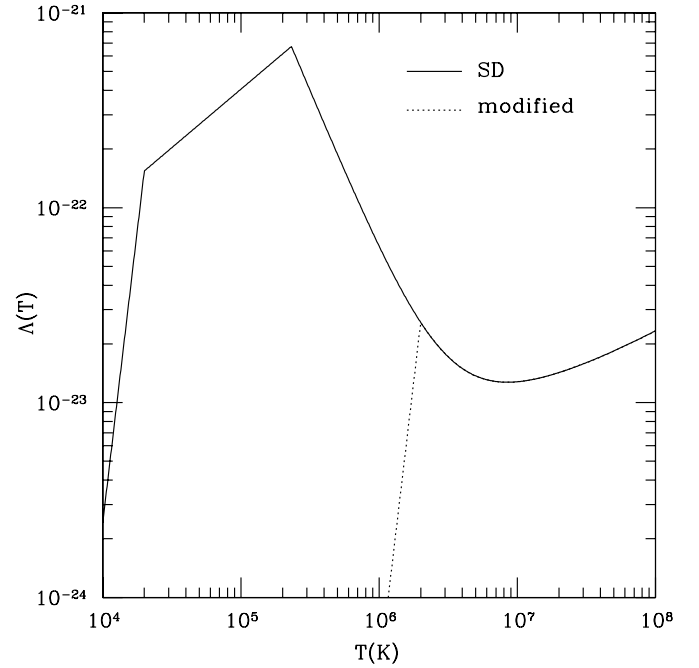


Figure 1. Cooling function vs. temperature. Solid line: fit to the Sutherland & Dopita cooling function for a third solar metallicity (Equation (12)). Dotted line: the modified cooling function used in our simulations which has a stable cold phase at $< 2 \times 10^6 \text{ K}$.

along the magnetic field, although the perpendicular conductivity is orders of magnitude larger than the microscopic value. In Section 4.3, we discuss how this artificially large perpendicular conductivity might affect the conclusions drawn from our simulations.

2.3. Numerical Simulations

In this paper, we carry out local one- and two-dimensional numerical simulations of thermal instability for conditions appropriate to the ICM. We use unstratified local patches of the ICM to isolate the physics of the thermal instability, as opposed to the buoyancy instabilities present in a stratified, conductive plasma (Balbus 2000; Quataert 2008). We focus on two-dimensional simulations—as opposed to three-dimensional simulations—because of the challenging numerical requirement of resolving the Field length in the cold medium (both parallel and perpendicular to magnetic field lines). Our box size is 40 kpc, somewhat larger than the typical Field length in the hot medium; we use periodic boundary conditions.

We use the publicly available ZEUS-MP code (Hayes et al. 2006) to solve the MHD equations. Thermal conduction along magnetic field lines is treated explicitly, using the method of Sharma & Hammett (2007) to prevent unphysical negative temperatures. Since the stable time step for conduction is much smaller than the MHD time step, thermal conduction is subcycled. The cooling and heating terms in Equation (4) are combined at each grid point, and internal energy is updated by a first-order explicit (semi-implicit) method if heating (cooling) dominates; this ensures that the internal energy is always positive, irrespective of the time step. Since the typical cooling time is much longer than the sound-crossing time across a grid cell, this first-order accurate treatment of cooling is sufficient.

Our initial condition consists of plasma with $T = 0.78 \text{ keV}$ and $n_e = 0.1 \text{ cm}^{-3}$; these parameters are characteristics of a reasonably dense, low entropy ($\simeq 3.6 \text{ keV cm}^2$) part of the

Table 1
One-dimensional Runs

Label ^a	Res.	Δx (kpc)	L_{\parallel} (kpc) ^b	f_m^c	f_V^c
HWC	1024	0.039	3.26	0.6	0.043
HNC	1024	0.039	0.22	0.9	0.07
HWCl	512	0.078	3.26	0.61	0.043
HWCh	2048	0.02	3.26	0.6	0.042
HWClI	256	0.16	0.89	0.67	0.043

Notes.

^a H stands for hydro, WC for with conduction. l and h stand for lower and higher resolution runs. Initially $n_e = 0.1 \text{ cm}^{-3}$, $T = 0.78 \text{ keV}$, so that the cooling time is $\approx 95 \text{ Myr}$. The Field length in the initial condition is $\approx 10 \text{ kpc}$ and at $2 \times 10^6 \text{ K}$ (temperature of the stable phase) is $\approx 0.07 \text{ kpc}$. The box size is 40 kpc.

^b L_{\parallel} is defined in Equation (14) and is evaluated at 1.43 Gyr, when the results have reached a quasi-steady state.

^c f_m (f_V) is the mass (volume) fraction of plasma below $5 \times 10^6 \text{ K}$ (the “cold phase”) evaluated at 1.43 Gyr.

ICM at small radii, deep in the cluster core. Note that the cooling time is longer than the sound crossing time across the box so that the thermal instability is in the roughly isobaric limit (except in magnetic/cosmic-ray-dominated regions, where it behaves isochorically; compare Equations (10) and (8)). We initialize homogeneous and isotropic $\sim 1\%$ isobaric density/temperature perturbations on this initial equilibrium state; the spectrum of initial perturbations is $\propto k$ for $k < k_0$ and $\propto k^{-1}$ for $k > k_0$, so that most of the power is initially at $\sim k_0$; k_0 corresponds to a scale $2\pi/k_0 \approx 0.8 \text{ kpc}$ for most of the simulations (we also experimented with smaller and larger k_0 for comparison). The exact spectrum of initial perturbations is somewhat arbitrary and is not well constrained in the ICM, but is also not crucial for the subsequent evolution. All of the simulations with the same k_0 have identical initial conditions and the initial conditions are smoothed/interpolated for lower/higher resolution simulations. This is important for quantitative testing of convergence with increasing resolution. The one-dimensional simulations do not include magnetic fields, while the initial magnetic field is $B = 5 \mu\text{G}$ and aligned at 45° to the box in the two-dimensional simulations. The simulations with cosmic rays begin with a uniform cosmic-ray pressure.

Tables 1 and 2 summarize the one- and two-dimensional simulations discussed in detail in this paper. The tables list the mass (f_m) and volume (f_V) fractions of plasma having a temperature below $5 \times 10^6 \text{ K}$ in the nonlinear state; this is a reasonable proxy for the mass and volume fractions of the cold phase. To quantify the spatial coherence of the structures in the nonlinear state of the thermal instability, we define the parallel and perpendicular length scales of the density field via

$$L_{\parallel} \equiv \frac{\int |\delta\rho| dV}{\int |\hat{\mathbf{b}} \cdot \nabla \delta\rho| dV} \quad (14)$$

and

$$L_{\perp} \equiv \frac{\int |\delta\rho| dV}{\int |(\hat{\mathbf{z}} \times \hat{\mathbf{b}}) \cdot \nabla \delta\rho| dV}, \quad (15)$$

where $\delta\rho = \rho - \langle \rho \rangle$, $\langle \rho \rangle$ is the volume-averaged density (which is constant in time because the mass in the computational domain is conserved), and $\hat{\mathbf{z}}$ is perpendicular to the simulation plane. For the one-dimensional simulations $\hat{\mathbf{x}}$ is used instead of $\hat{\mathbf{b}}$ in Equation (14) and L_{\perp} is not defined, so we only provide L_{\parallel} in Table 1.

3. ONE-DIMENSIONAL SIMULATIONS

Figure 2 shows temperature profiles in the linear (left) and nonlinear (right) regimes for one-dimensional hydrodynamic simulations with (HWC) and without (HNC) thermal conduction. For the simulation without conduction (dotted line) the temperature fluctuations grow at all scales in the linear regime. By contrast, for the run with conduction (dashed line) modes with scales smaller than the Field length are suppressed by thermal conduction and only the large-scale modes grow. Nonlinearly, the cold phase is compressed into a smaller and smaller volume with time in the absence of conduction, until the cold phase is unresolved (note that L_{\parallel} in Table 1 is much smaller for the run without conduction compared to the runs with conduction); the cold peaks also merge, reducing the total number of dense peaks in time (compare profiles at 1.43 and 1.91 Gyr for HNC in the right panel of Figure 2). Eventually all of the cold peaks will merge and approach the grid scale because there is no heating of the cold phase to prevent this. As the cold phase accumulates more and more mass in time, the negligible mass in the hot phase becomes hotter and hotter to conserve energy (which is enforced in our simulations via the heating term $H(t)$ in Equation (4)).

The nonlinear evolution with conduction is qualitatively different: there is only one cold region (this is because of the large Field length in the initial plasma; this result is insensitive to the initial density fluctuation spectrum) and the hot phase saturates at a temperature $\approx 2 \text{ keV}$, much cooler than in the simulations without conduction. The temperature of the cold phase is, however, the same with and without conduction; this is set by the temperature of the thermally stable branch of the cooling function. Figure 2 shows that in the presence of conduction, the temperature profile reaches an approximate steady state, with very little change from 1.43 to 1.91 Gyr. The steady state requires both the additional heating $H(t)$ in Equation (4) and thermal conduction. In particular, the cooling is dominated by the dense, cold gas while the extra heating is primarily supplied to the hot phase (because H is constant per unit volume). This extra heating is conducted to the rapidly cooling ($\propto n^2$) cold phase producing a steady state. This energy transfer from the hot to the cold phase can only be properly captured if the Field length in the cold phase is resolved, which is why it is critical to do so to obtain converged results (see Koyama & Inutsuka 2004).

Figure 3 shows temperature profiles at 1.43 Gyr for simulations including thermal conduction at several different resolutions. The temperature profile is reasonably converged only for simulations with more than 512 grid points; in particular, note that the physical size of the cold phase does not change with resolution for $N > 512$. This is only true when the Field length in the cold phase is resolved. The Field length for the initial temperature and density is $\approx 10 \text{ kpc}$. The Field length for the isobaric cold phase at $2 \times 10^6 \text{ K}$ (the stable phase for our modified cooling curve; Figure 1) is $\approx 0.07 \text{ kpc}$; this just starts to be resolved at more than 512 grid points since our box size is 40 kpc, and thus $\Delta x = 0.078 \text{ kpc}$ at $N = 512$.

4. TWO-DIMENSIONAL SIMULATIONS

Having used one-dimensional simulations to describe the basic physics of the thermal instability and the numerical requirements for simulating it, we now turn to the more physically realistic case of two-dimensional simulations. As we have emphasized previously, the Field length must be

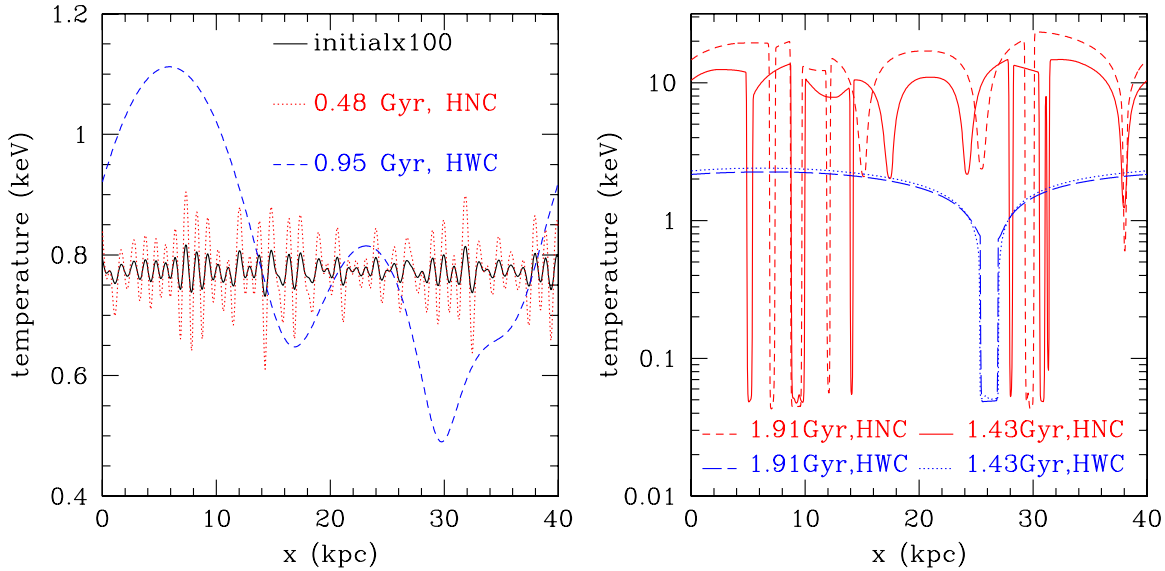


Figure 2. Temperature profiles for one-dimensional runs with (HWC) and without (HNC) conduction at different times in the linear (left) and nonlinear (right) regimes. The initial temperature fluctuations have been multiplied by a factor of 100 for clarity.

(A color version of this figure is available in the online journal.)

Table 2
Two-dimensional Runs

Label ^a	Res.	$\Delta x = \Delta y$ (kpc)	p_{cr}/p	D_{\parallel} (cm 2 s $^{-1}$)	$\frac{\langle \text{heating} \rangle}{\langle \text{cooling} \rangle}$	L_{\parallel}/L_{\perp} ^c	f_m ^d	f_V ^d
MWC ^b	1024	0.039	0	...	1	2.48	0.51	0.061
MWCl	512	0.078	0	...	1	2.18	0.5	0.06
MWCh	2048	0.02	0	...	1	2.55	0.51	0.064
MWIC	1024	0.039	0	...	1	1.08	0.48	0.041
MWCCR	1024	0.039	0.1	0	1	3.45	0.41	0.12
MWCCRs	1024	0.039	10^{-3}	0	1	2.5	0.5	0.063
MWCCRd28	1024	0.039	0.1	10^{28}	1	2.66	0.4	0.1
MWCCRd30	1024	0.039	0.1	10^{30}	1	2.29	0.47	0.061
MWCh0.9c	1024	0.039	0	...	0.9	3.91	0.9	0.38
MWCh1.05c	1024	0.039	0	...	1.05	3.86	0.018	1.5×10^{-3}

Notes.

^a M stands for MHD. WC means with conduction, IC is for isotropic conduction, CR for cosmic rays. l and h stand for lower and higher resolution runs. All runs have a small isotropic conduction added for convergence (see Section 2.2). Initially $n_e = 0.1 \text{ cm}^{-3}$ and $T = 0.78 \text{ keV}$, so that the cooling time is $\approx 95 \text{ Myr}$. Initial magnetic field is $5 \mu\text{G}$ and aligned 45° to the two-dimensional Cartesian box. The Field length in the initial condition is $\approx 10 \text{ kpc}$ and at $2 \times 10^6 \text{ K}$ (temperature of the stable phase) is $\approx 0.07 \text{ kpc}$. The box size is 40 kpc . Some less crucial simulations are not included in the table but are discussed in the text.

^b The fiducial run.

^c L_{\parallel} and L_{\perp} are defined in Equations (14) and (15), and are evaluated at 0.95 Gyr.

^d f_m (f_V) is the mass (volume) fraction of plasma below $5 \times 10^6 \text{ K}$ (the “cold phase”) evaluated at 0.95 Gyr (except for MWIC where these are evaluated at 1.43 Gyr).

resolved both parallel and perpendicular to the local magnetic field in multi-dimensional simulations of the thermal instability. This is why we (1) include an isotropic thermal conductivity (which helps resolve structures perpendicular to the field; see Section 2.2) in addition to the parallel conductivity and (2) artificially increase the temperature of the thermally stable phase (Figure 1).

4.1. The Fiducial Run: MHD with Anisotropic Thermal Conduction

Our fiducial two-dimensional simulation is MWC summarized in Table 2; this is an MHD simulation with anisotropic thermal conduction and an initial magnetic field of $B = 5 \mu\text{G}$ aligned at 45° relative to the x -axis, in the plane of the simulation. The initial density (0.1 cm^{-3}) and temperature (0.78 keV) correspond to an initial cooling time of 95 Myr and a

length $\approx 10 \text{ kpc}$ along the magnetic field and $\approx 1.7 \text{ kpc}$ perpendicular to the field; the magnetic field initially contributes only $\approx 0.4\%$ ($\beta = 8\pi p/B^2 \approx 250$) of the total pressure. Figure 4 shows contour plots of the temperature in the linear (0.475 Gyr) and nonlinear (0.95, 1.425 Gyr) regimes, along with arrows showing the magnetic field direction at each time; because the pressure remains relatively constant even nonlinearly, density scales nearly as the inverse of temperature.

Figure 4 shows that the thermal instability develops anisotropically, with a filamentary structure along the magnetic field; this is because thermal conduction efficiently suppresses small-scale structures along the field, but not across it. Quantitatively, the ratio L_{\parallel}/L_{\perp} measures the anisotropy of filaments with respect to the magnetic field; this is ~ 2.5 at 0.95 Gyr (Table 2) and increases to ~ 3.5 at later times (see the left panel in Figure 11). The number of cold filaments decreases in time because some of the filaments merge together nonlinearly. Interestingly, the

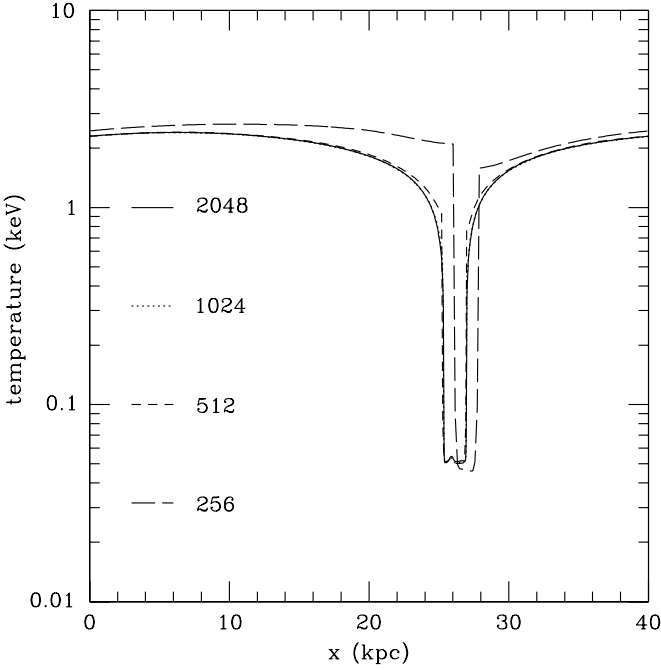


Figure 3. Temperature profiles for one-dimensional simulations with conduction at $t = 1.43$ Gyr for different resolutions: HWCl (256), HWCl (512), HWC (1024), and HWCh (2048). Convergence is achieved for > 512 grid points.

majority of the cold filaments are oriented along the direction of the local magnetic field even in the nonlinear regime. Some of the filaments at 0.95 Gyr are quite small and relatively isotropic because of small and nearly isotropic conduction in the cold phase. However, at later times (e.g., 1.425 Gyr) the small filaments coalesce to form large ones. The nonlinear development of the thermal instability proceeds in two phases: in the first phase nonlinear filaments aligned along field lines condense from the hot ICM, becoming shorter in time because of a smaller conductivity in the cold phase; in the second stage these cold filaments with large velocities (primarily along themselves) merge to form longer filaments. This is clearly seen in Figure 11 as an increase in L_{\parallel}/L_{\perp} after an initial dip at ~ 1 Gyr.

Figure 4 shows that the direction of the magnetic field is only moderately perturbed from its initial direction even in the fully nonlinear regime. However, the magnetic field strength increases by a factor of $\gtrsim 3\text{--}8$ in the cold filaments (see the left panel of Figure 5), to the point where the magnetic pressure is important in the filaments. The regions over which the field is enhanced are coincident with, but significantly longer than, the location of the cold filaments. The field enhancement occurs via flux freezing as the cooling plasma is compressed perpendicular to the initial field direction in the nonlinear state

of the thermal instability; analogous compression along the field lines is suppressed because of thermal conduction. In the hot diffuse gas between the filaments, the magnetic field decreases by a factor $\simeq 2\text{--}3$ from its initial value of $\approx 5 \mu\text{G}$. Note that for a realistic cooling function, the density contrast between the filaments and the diffuse medium will be larger than is found in our simulations, and so the magnetic field compression in the filaments will also be stronger.

The right panel of Figure 5 shows that the velocities driven by the thermal instability can reach $30\text{--}100 \text{ km s}^{-1}$, comparable to the sound speed in the cold filaments, but much less than the sound speed in the hot phase. Such high velocities can disrupt the tendency of buoyancy instabilities in the hot phase of the ICM to reorient the magnetic field (e.g., Sharma et al. 2009b; Parrish et al. 2010). The high velocities are spatially coincident with the magnetic field enhancements and the cold filaments. The velocity vectors generally point toward the cold filaments in the hot phase, showing that mass from the hot thermally unstable medium is condensing into the cold phase. This flow of mass is, however, transient. The thermal instability reaches a steady state in which cooling from the dense, cool ICM is balanced by conductive heating from the hot ICM, which is in turn heated (artificially) by our external heat source $H(t)$ in Equation (4). Once this steady state is established, mass flow between the phases is significantly reduced. Although mass flow across the phases is reduced, the cold filaments retain large velocities along themselves and the volume-averaged velocity is $\sim 20 \text{ km s}^{-1}$ (see the right panel of Figure 11 discussed later).

Nonlinearly, the plasma exists in two phases, with very little plasma at the intermediate temperatures. Figure 6 shows the mass (left panel) and volume (right panel) distribution of plasma at different times for the fiducial run. The plasma is at $\approx 10^7 \text{ K}$ initially but evolves into a two-phase structure. The phase structure evolves rapidly at early times (before ~ 1 Gyr), but the evolution is slower at later times. The mass and volume occupied by the plasma at intermediate temperatures decrease in time. The “mass dropout rate,” (i.e., the rate at which plasma cools below a given temperature) at 10^7 K is large initially, but once a two-phase medium is established, the mass and volume of the hot and cold phases are roughly constant in time, with very little mass dropout. While there is significant mass in the cold filaments, most of the volume is occupied by the hot phase (see f_m and f_v in Table 2). The hottest plasma in the domain slowly becomes hotter with time in the two-dimensional simulations; by contrast, in one dimension the plasma reaches a steady state at 1.43 Gyr (Figure 2). It takes longer to reach a quasi-steady state in two dimensions because it is easier for hot isothermal regions to become thermally isolated from the cold plasma (because of the small perpendicular conductivity). Since the

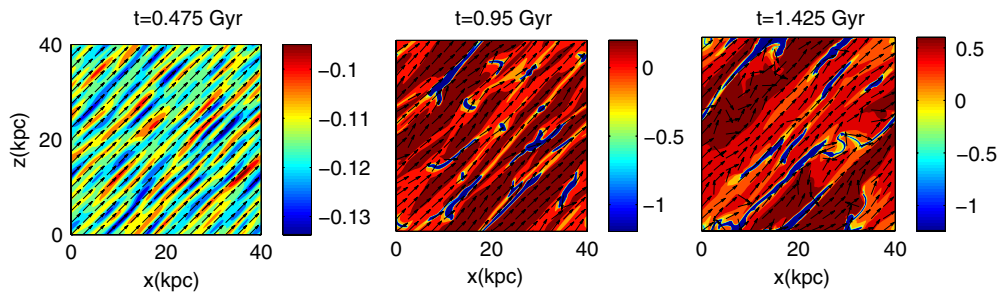


Figure 4. Contour plots of \log_{10} temperature (in keV) for the fiducial run (MWC) at linear (0.475 Gyr; left) and nonlinear (0.95 Gyr, center; 1.425 Gyr, right) stages of the instability. The arrows show the magnetic field direction.

(A color version of this figure is available in the online journal.)

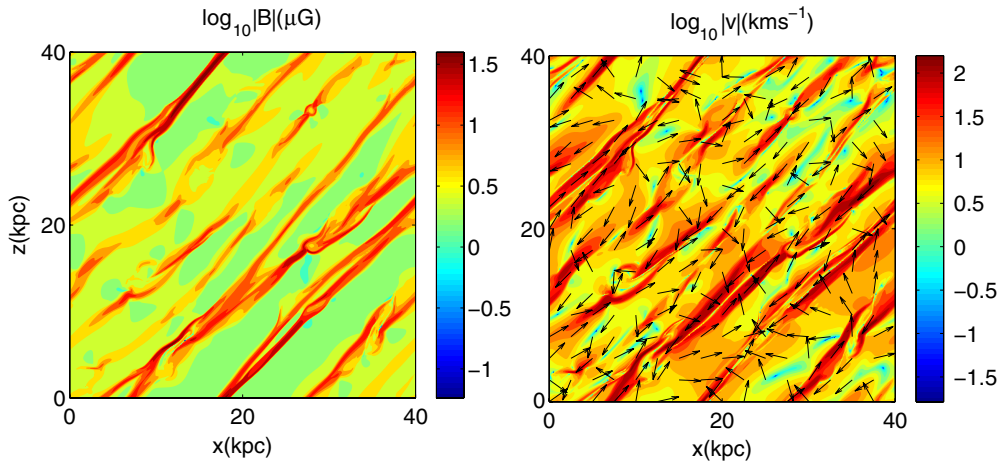


Figure 5. Contour plots showing $\log_{10}|B|$ (magnitude of the magnetic field strength; left) and $\log_{10}|v|$ (magnitude of the velocity; right) for the fiducial run at 0.95 Gyr. The arrows in the velocity plot show the direction of the velocity unit vector.

(A color version of this figure is available in the online journal.)

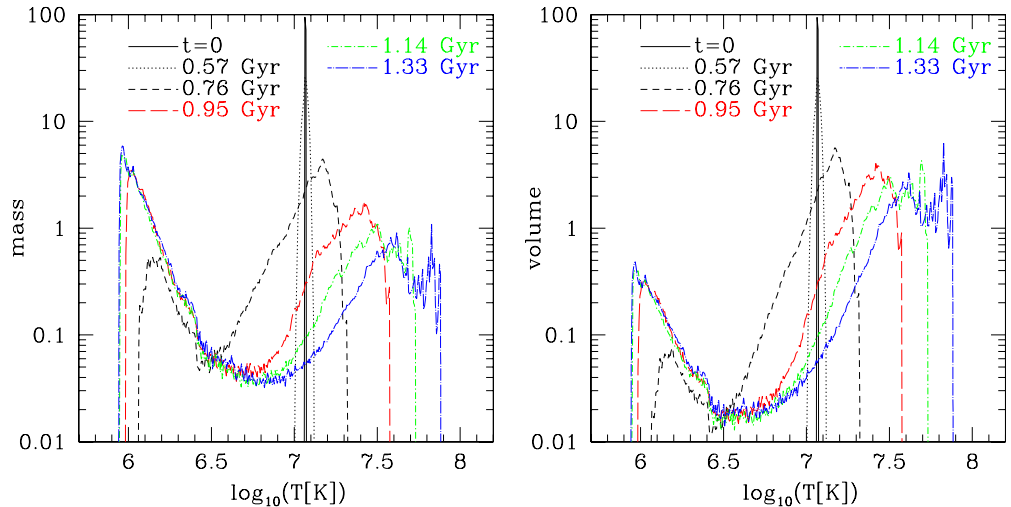


Figure 6. Mass ($dM/d \log_{10} T$; left) and volume ($dV/d \log_{10} T$; right) fractions occupied by plasma of a given temperature T for the fiducial run (MWC) at different times. The normalization is such that the total mass/volume under the curve is unity. The initial cooling time is ≈ 0.1 Gyr and the simulations begin to saturate after ≈ 0.8 Gyr. The hottest plasma in the box becomes hotter with time.

(A color version of this figure is available in the online journal.)

hottest plasma becomes hotter with time and the conductivity is a strong function of temperature (Equation (11)), it becomes difficult to run the simulations for long times.

4.2. Simulations with Isotropic Thermal Conduction

To assess the importance of including anisotropic thermal conduction, we carried out simulations identical to the fiducial run in every way except that the conductivity is isotropic at the Spitzer value (MWIC in Table 2). Figure 7 shows the temperature contour plots at 0.475 Gyr (left panel) and 0.95 Gyr (right panel). In the linear state the modes are isotropic and on relatively large scales, irrespective of the magnetic field direction. By contrast, with anisotropic conduction, the cold plasma is filamentary even in the linear state (Figure 4).²

² The Field length perpendicular to the magnetic field is much smaller in the simulation with anisotropic conduction than in the simulation with isotropic conduction. This is why there is much more small-scale structure, and more cold “filaments,” in Figure 4 than in Figure 7. In addition, because we initialize power primarily at ≈ 0.8 kpc (Section 2.3), the amplitude of the initial perturbations that can actually grow (\gtrsim the Field length) is larger in the simulation with anisotropic conduction. These perturbations thus evolve somewhat more rapidly.

Nonlinearly, the orientation of the cold plasma in simulations with isotropic conduction is unrelated to—or even somewhat perpendicular to (see the dotted line in Figure 8)—the local magnetic field direction, unlike in simulations with anisotropic conduction, where the filaments develop along the magnetic field (Figure 4). Although the morphology of the cold gas is different in the two cases, the evolution of the phase structure is qualitatively similar; there is significant mass in the cold phase, but the volume is dominated by the hot phase. The differences between Figures 4 and 7 emphasize the critical importance of including anisotropic thermal conduction when studying the thermal physics of galaxy cluster plasmas.

4.3. Convergence of Two-dimensional Simulations

As described previously, in multi-dimensional simulations, the Field length must be resolved both along and perpendicular to the direction of the magnetic field in order for the numerical results to converge. Figure 9 shows temperature contour plots at 0.95 Gyr for runs including perpendicular conduction, with 2048 and 512 grid points, respectively. The temperature contour plots are reasonably similar, and are similar to the results for

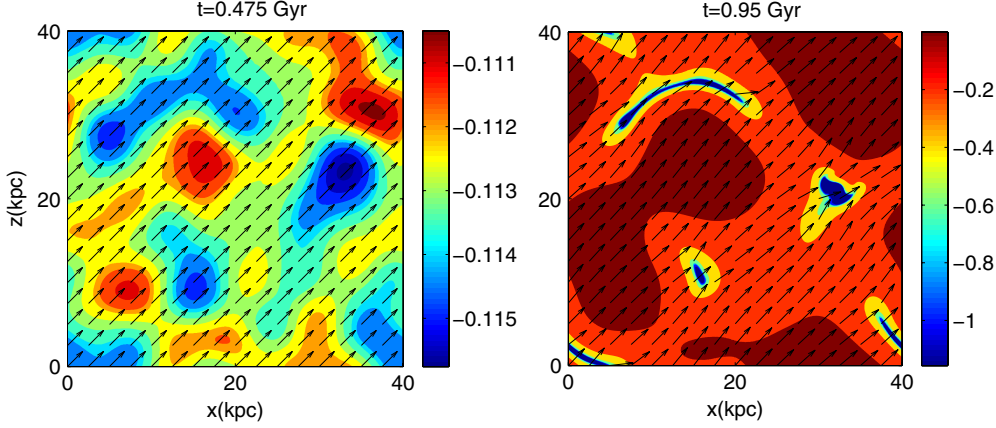


Figure 7. Contour plots of \log_{10} temperature (keV) for the simulation with isotropic thermal conduction at the Spitzer value (MWIC), at 0.475 Gyr (left) and 0.95 Gyr (right). The arrows show the magnetic field direction.

(A color version of this figure is available in the online journal.)

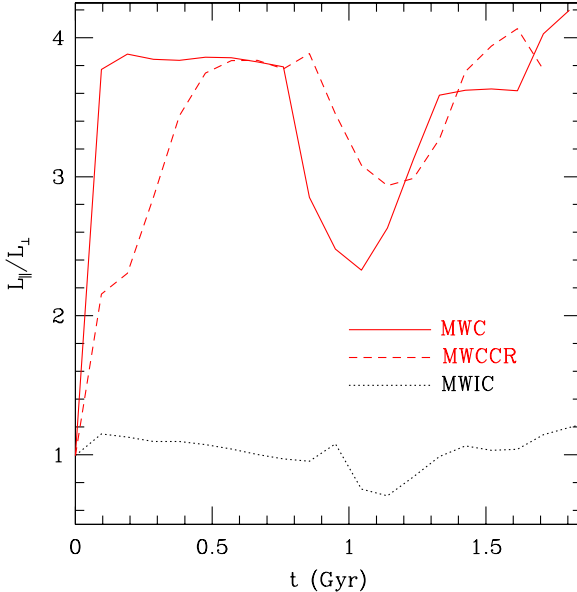


Figure 8. Anisotropy of the density field L_{\parallel}/L_{\perp} as a function of time for different runs: the fiducial run (MWC), the run with initial $p_{\text{cr}}/p = 0.1$ (MWCCR), and the run with isotropic conduction (MWIC). Note also that the filaments are longer and broader for simulations that include cosmic rays, i.e., both L_{\parallel} & L_{\perp} are larger even though L_{\parallel}/L_{\perp} is comparable (see Figures 4 and 12).

(A color version of this figure is available in the online journal.)

$N = 1024$ in Figure 4. Figure 11 provides a more quantitative test of the convergence of the simulations: it shows that the volume-averaged values of L_{\parallel}/L_{\perp} (the anisotropy of the filaments) and $\langle |v| \rangle$ (the random velocity) are almost the same, irrespective of resolution, for runs with perpendicular conduction (labeled “Y”).

To explicitly illustrate the importance of including thermal conduction perpendicular to field lines for convergence, we carried out simulations similar to the fiducial run, but without the small isotropic conductivity. Figure 10 shows temperature contour plots for simulations without perpendicular conduction, for $N = 2048$ and 512 grid points. In this case, the two different simulations give very different results; in particular the filaments are much thinner and the number of filaments is much larger (by a factor ~ 4) for the higher resolution run. This is also seen in the left panel of Figure 11 which shows that the anisotropy of the filaments L_{\parallel}/L_{\perp} increases with increasing resolution for

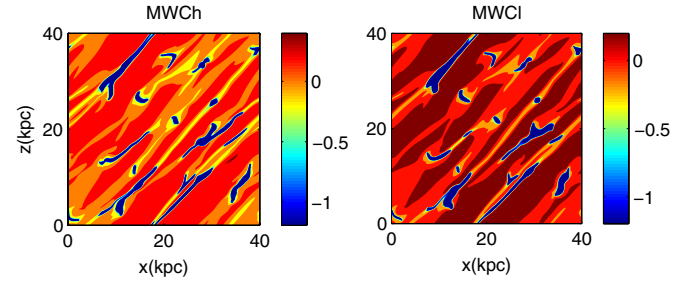


Figure 9. Contour plots of \log_{10} temperature (keV) at 0.95 Gyr for higher (MWCh; left) and lower (MWCI; right) resolution analogs of our fiducial run. Figure 4 shows the corresponding temperature plot for the fiducial run. All three are reasonably similar.

(A color version of this figure is available in the online journal.)

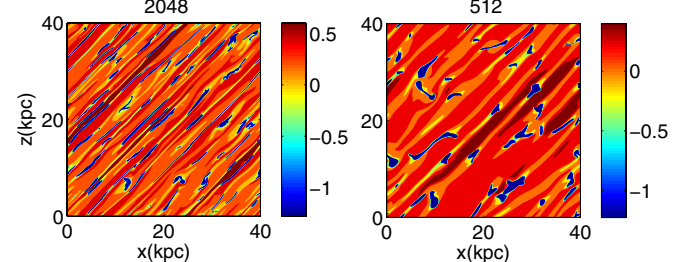


Figure 10. Contour plots of \log_{10} temperature (keV) at 0.95 Gyr for high (2048; left) and low (512; right) resolution simulations without the small isotropic conductivity which is needed for convergence. Compare with Figure 9, which shows results for simulations including a small isotropic conductivity.

(A color version of this figure is available in the online journal.)

runs without perpendicular conduction. Similarly, the volume-averaged velocity ($\langle |v| \rangle$) does not show clear convergence with increasing resolution in the absence of the isotropic conductivity (see the right panel of Figure 11).

It is important to stress that the simulations with perpendicular conduction (e.g., Figure 9) significantly overestimate the thickness of the filaments perpendicular to the magnetic field, because the perpendicular conductivity is too large by orders of magnitude. In this sense the trend in Figures 11 and 10 is correct, namely the perpendicular structures should indeed be thinner than in our fiducial simulations. However, it is critical that the Field length be resolved perpendicular to the magnetic field, or else spurious numerical results can arise (e.g., in our simulations with cosmic rays, we found that the cosmic-ray pressure

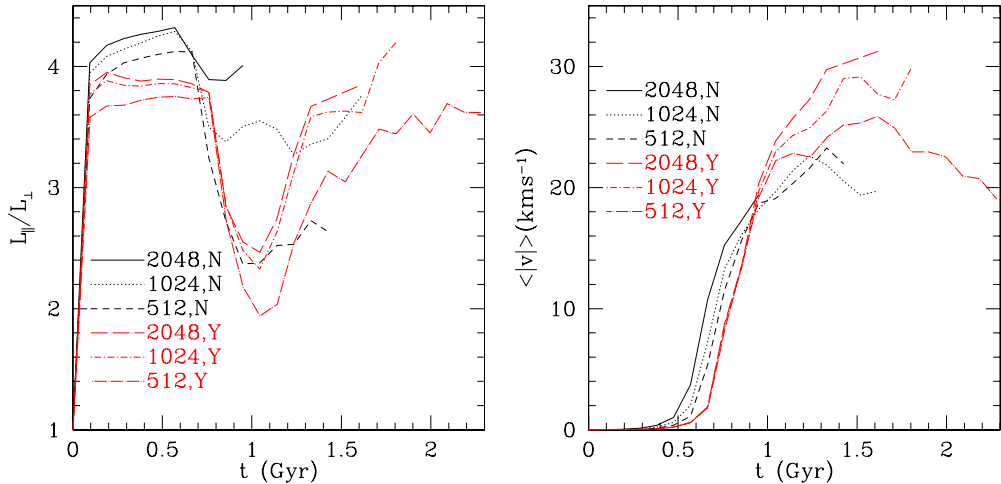


Figure 11. Left: volume-averaged filament anisotropy (L_{\parallel}/L_{\perp} ; Equations (14) and (15)) as a function of time. Right: volume-averaged random velocity as a function of time. In both cases, we show simulations with (labeled “Y”) and without (labeled “N”) a small isotropic conductivity (see Section 2.2). Simulations with the isotropic conduction converge reasonably well with increasing resolution (for $N > 512$; also see Figure 3) but those without it do not. We could not run the higher (2048) resolution simulations for long because of very limiting time-step constraints.

(A color version of this figure is available in the online journal.)

could become spuriously large in cold filaments when they were not properly resolved, even if the initial cosmic-ray pressure was negligible). Physically, small-scale turbulent heat transport (e.g., due to Kelvin–Helmholtz instabilities at the boundaries of the filaments) or other physics (e.g., cosmic-ray pressure; Section 4.4) probably sets the perpendicular scale of the filaments, not the true microscopic perpendicular heat transport. These processes are not currently well understood and it is unclear to what extent they can simply be treated as an enhanced perpendicular conductivity (as we have done here).

4.4. Effects of Cosmic Rays on Filament Formation

In the previous sections, we have highlighted the dynamics and thermodynamics of the thermal plasma during thermal instability. In this section, we consider the role of cosmic rays, i.e., a non-thermal population of particles. Figure 12 shows contour plots of the ratio of the cosmic-ray to plasma pressure for simulations with two different initial cosmic-ray pressures, $p_{\text{cr}}/p = 0.1$ and 10^{-3} , respectively; the cosmic rays are adiabatic in these simulations. Figure 12 shows that the cosmic rays become concentrated in the cold filaments; this is because the cosmic-ray entropy $p_{\text{cr}}/\rho^{4/3}$ is conserved and the cosmic rays are thus compressed along with the thermal plasma into the cold filaments. For the simulations with a very small cosmic-ray pressure (the right panel of Figure 12), the properties of the thermal plasma in the filaments and in the diffuse ICM are very similar to those in the simulations without cosmic rays (Figure 4). In particular, because the cosmic-ray pressure is small even in the nonlinear state, the cosmic rays do not affect the physics of how the filaments form. On the other hand, when the initial cosmic-ray pressure is larger (the left panel of Figure 12), adiabatic compression of the cosmic rays in the filaments leads to cosmic-ray pressure dominated filaments that are longer and broader than in the absence of cosmic rays; the additional cosmic-ray pressure halts the contraction of the filaments when $p_{\text{cr}} \sim p$.

Table 2 shows that the volume fraction f_V of the cold phase is larger for simulations in which the filaments are cosmic ray dominated (MWCCR and MWCCRd28); the mass fraction f_m , however, is smaller. This is because of the smaller gas density and thermal pressure in the cold filaments. In addition,

Figure 8 shows (short dashed line) that the filaments are more anisotropic (L_{\parallel}/L_{\perp} is larger) in the nonlinear phase for cosmic-ray-dominated filaments; this is because the cosmic-ray pressure resists parallel compression. Indeed, a visual comparison of the filaments with and without a large cosmic-ray pressure in Figure 12 shows that the absolute parallel length scale of the filaments is larger when the cosmic rays are dynamically important.

For a realistic cooling function, the density contrast between the filaments and the thermal plasma is much larger than in our simulations (because the stable thermal phase has $T \simeq 10^4$ K rather than $T \simeq 2 \times 10^6$ K). For an initial ICM temperature of $\sim 10^7$ K, the real density contrast should be $\sim 10^3$ at a fixed pressure (assuming the filaments are not cosmic-ray pressure dominated). Thus, even with an initially very small cosmic-ray pressure in the ICM of $p_{\text{cr}}/p \sim 10^{-4}$, the cosmic rays can be adiabatically compressed to be dynamically important in filaments. This suggests that the cosmic-ray-dominated results in the left panel of Figure 12 are likely to be the most physically realistic. However, for the large gas densities and cosmic-ray pressures that obtain in the filaments, cosmic ray losses due to ionization, pion production, and cosmic-ray streaming will become important. The hadronic and ionization loss timescales are comparable, $\approx 200/n_e(\text{cm}^{-3})$ Myr, for relativistic protons with kinetic energy of a few GeV (e.g., Schlickeiser 2002). The energy loss timescale because of cosmic-ray streaming is roughly the Alfvén crossing time along the filament (~ 1 Gyr for a 10 kpc long filament and an Alfvén speed of 10 km s^{-1}). Since these loss timescales are only modestly longer than the nominal cooling time, and since the filaments are expected to be dense, cosmic-ray losses have to be included self-consistently. While including ionization and hadronic losses is straightforward, numerically implementing cosmic-ray streaming is non-trivial (see Sharma et al. 2009c). A self-consistent treatment of this physics is beyond the scope of the present paper, but may modify the impact of cosmic rays on filament formation.

The only non-adiabatic cosmic-ray physics in our calculations is diffusion along magnetic field lines (Equation (5)). Our calculations with different parallel diffusivities D_{\parallel} show that, so long as $D_{\parallel} \lesssim 10^{29} \text{ cm}^2 \text{ s}^{-1}$, the adiabatic results in Figure 12 are reasonably applicable. Sharma et al. (2009a) presented general

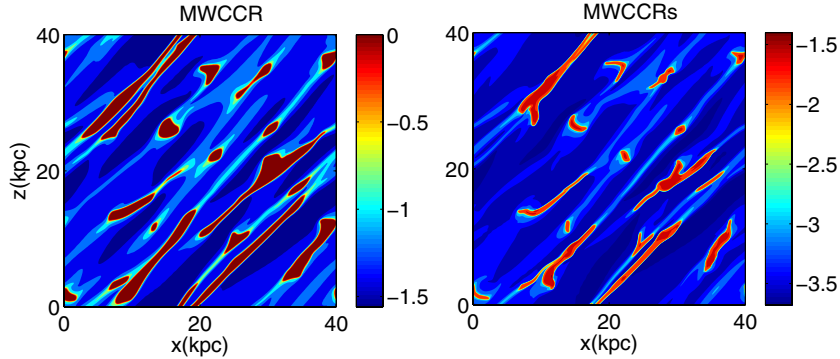


Figure 12. Contour plots of the cosmic-ray to plasma pressure ratio, $\log_{10}(p_{\text{cr}}/p)$, at 0.95 Gyr for the runs with initial $p_{\text{cr}}/p = 0.1$ (MWCCR; left) and initial $p_{\text{cr}}/p = 10^{-3}$ (MWCCRs; right). The density/temperature contour plots look similar to these because $p_{\text{cr}}/\rho^{4/3}$ is conserved.

(A color version of this figure is available in the online journal.)

arguments that the diffusivity is likely to satisfy this inequality, so we suspect that large cosmic-ray pressures in filaments are the norm. There are indeed observational indications that this is the case (e.g., the modeling of atomic and molecular lines by Ferland et al. 2009); we will discuss this comparison in Section 5.

4.5. Simulations with Different Cooling/Heating Functions

To understand which aspects of the nonlinear evolution of the thermal instability in the ICM are robust, we have carried out similar calculations to those reported here with different assumptions about the heating and/or cooling functions. Recall that the heating function is particularly poorly constrained in the ICM. To give one example, we carried out a series of simulations with the heating proportional to density, i.e., with a heating that is constant per unit mass instead of constant per unit volume as in our fiducial models shown here. The results were qualitatively similar to the fiducial case, with anisotropic filaments and most of the volume in the hot phase. Nonlinearly, the mass fraction in the cold phase (0.38 at 1.9 Gyr) is smaller than in the fiducial run. The cold phase is slightly hotter ($\approx 2 \times 10^6$ K instead of $\approx 10^6$ K in the case of the fiducial run; see Figure 6) and has a smaller spread in temperature than in the fiducial run, and it takes longer for nonlinear saturation because the cold phase is heated more effectively than in the fiducial case. The aspect ratio of the cold filaments (measured by L_{\parallel}/L_{\perp}) is similar to the fiducial run.

We also carried out simulations in which the volume-averaged instantaneous heating rate was not equal to the cooling rate: random perturbations (up to 200%) in both space and time were added to the volume-averaged heating rate. These runs also showed results qualitatively similar to the fiducial run, except that the field lines were more disturbed from the initial configuration, and the mass and volume fractions of plasma at intermediate temperatures were larger (as would be expected). This demonstrates that the existence of a multiphase medium and cold filaments aligned along the magnetic field are robust consequences of thermal instability in the ICM. The only way out of these conclusions is if there is a heating mechanism that is *locally* thermally stable on scales \gtrsim the Field length; this is a much more stringent requirement to satisfy than the global thermal stability of the ICM (however, see Kunz et al. 2010).

The fiducial run (and all other runs) uses the modified cooling curve shown in Figure 1 with the stable phase at $T < 2 \times 10^6$ K. To assess what happens to filaments with a realistic cooling function, in which the stable phase is at

$< 10^4$ K, we carried out two runs (with and without cosmic rays) in which the stable phase of the cooling curve exists for $T < 10^6$ K. The Field length in the stable phase of these simulations is ≈ 8 times smaller than in our fiducial calculations (see Equation (13)). For this reason these runs are only barely resolved (see Section 3, 4.3 for discussion of convergence), but they nonetheless indicate the trends expected for a more realistic cooling function. Nonlinearly, the run with cosmic rays shows much longer (and broader) filaments than the run without cosmic rays. This can also be seen by comparing the filaments in Figure 4 (for the fiducial run) and Figure 12 (for the run with cosmic rays MWCCR; see also Figure 8); however, the difference is even more dramatic for the runs with a cooler stable phase. For a smaller stable phase temperature, simulations without cosmic rays have very narrow and short filaments, while in simulations with cosmic rays the sizes of filaments do not depend significantly on the stable phase temperature. Thus, adiabatically compressed cosmic rays, which dominate the pressure in the filaments, are likely able to prevent compression of the cold plasma to very small scales for a realistic cooling function.

4.6. Runs with Heating \neq Cooling

In cluster cores the instantaneous heating rate is probably not identically equal to the cooling rate, as we have assumed in our models. However, the inferred global stability of clusters suggests that for timescales longer than a few cooling times heating does roughly balance cooling. Otherwise, all of the plasma will be in the cold phase (if cooling dominates) or in the hot phase (if heating dominates). To test the sensitivity of the phase structure to the degree of imbalance between heating and cooling, we carried out simulations in which heating does not quite balance cooling (Table 1). Figure 13 shows temperature contour plots after $\gtrsim 0.95$ Gyr for simulations with a constant heating per unit volume $= 0.9 \times$ cooling (MWCh0.9c) and with heating per unit volume $= 1.05 \times$ cooling (MWCh1.05c). The two plots differ dramatically. When cooling is somewhat stronger than heating (MWCh0.9c), the filaments are longer, much broader, and contain more of the mass, as compared to the fiducial run; by contrast, when heating exceeds cooling (MWCh1.05c), the cold structures are much smaller. The results differ even more dramatically from our fiducial calculations for a larger imbalance between heating and cooling. When heating does not exactly balance cooling, there will only be a single phase if we wait long enough. The relevant timescale is $t_{\text{sec}} \approx t_{\text{cool}} C / |C - H|$, the timescale for secular heating/cooling

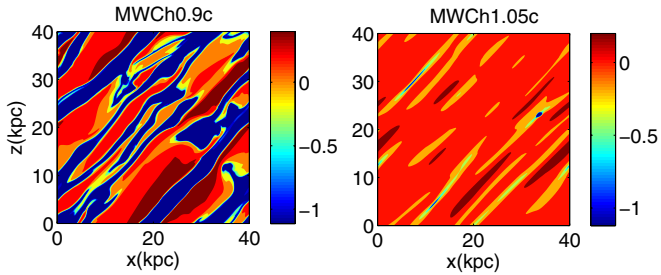


Figure 13. Contour plots of \log_{10} temperature (keV) at 0.95 Gyr for the run with volume-averaged heating = $0.9 \times$ volume-averaged cooling (MWCh0.9c; left) and for the run with volume-averaged heating = $1.05 \times$ volume-averaged cooling (MWCh1.05c; right).

(A color version of this figure is available in the online journal.)

of the plasma, where H/C is the volume-averaged heating/cooling rate. After $\sim t_{\text{sec}}$ the plasma will be dominated by hot/cold phase if heating/cooling dominates. Note that Figure 13 is shown at $\simeq 0.95$ Gyr, which is $\sim t_{\text{sec}}$ for these models. The fact that many cluster cores show a multiphase structure implies that heating balances cooling over a few cooling times. In the future, a more quantitative comparison between simulations like those reported here and observations might provide interesting constraints on the degree of thermal balance in cluster cores.

5. ASTROPHYSICAL IMPLICATIONS

Early thermal stability analyses of galaxy clusters were done within the context of the cooling flow model, in which mass inflows on the same timescale that the plasma cools; this can significantly modify the physics of the thermal instability (e.g., Balbus & Soker 1989). However, observations now clearly demonstrate the lack of significant cooling flows; a poorly understood source of heating (plausibly a central AGN) roughly balances cooling, maintaining approximate global thermal stability. In spite of their global stability, clusters can still be vulnerable to local thermal instability whenever Field's criterion is satisfied (i.e., whenever there are growing solutions to Equation (8)). Thermal conduction helps stabilize cluster plasmas on scales smaller than the Field length (Equation (9)), so it is the larger scale perturbations that are particularly prone to instability. It is not guaranteed that such instabilities in fact exist: whether they do depend on the details of how the plasma is heated. In this paper, we have used two-dimensional MHD simulations with anisotropic conduction and cosmic rays to study the nonlinear dynamics of thermal instability for conditions appropriate to galaxy clusters, under the assumption that local heating is not able to maintain thermal stability. Our results can only be semi-quantitatively applied to observed clusters, given current uncertainties in the heating physics. Nonetheless, we find that none of our conclusions are that sensitive to the precise form of the heating function (e.g., whether it is constant per unit mass or constant per unit volume; Section 4.5). We also find similar results in simulations that include a slight imbalance between heating and cooling (so long as the simulation is not run too long; Section 4.6) or random perturbations in the heating/cooling rates on top of a thermal balance (Section 4.5). Observations of atomic and molecular filaments and star formation in cool cluster cores (e.g., Cavagnolo et al. 2008; O'Dea et al. 2008) provide observational evidence for local thermally unstable regions in clusters.

Our calculations show that, for numerical convergence, the Field length in the *cold* medium needs to be resolved not only along the magnetic field, but also perpendicular to the field lines. To do so, we have artificially increased the temperature at which the plasma is thermally stable on the low temperature part of the cooling curve (to 2×10^6 K; see Figure 1). We have also included a small isotropic thermal diffusivity, to ensure that the perpendicular Field length is resolved (Section 2.2).

During the evolution of the thermal instability, rapid thermal conduction along magnetic field lines suppresses compression of plasma along the field at scales smaller than the Field length. However, compression occurs perpendicular to field lines on large scales, where magnetic tension is not important. Thus, if the Field length is \lesssim the size of a galaxy cluster core, and if the cooling time is short compared to the age of the cluster, the ICM is likely to be multiphase, with atomic filaments aligned with the local magnetic field. Note that this conclusion holds even in the fully nonlinear regime and does *not* require dynamically strong magnetic fields (Figure 4). Rather, thermal instability leads to a filamentary structure because of the poor heat transport across magnetic fields. This result implies that the orientation of atomic filaments can provide a local measure of the magnetic field direction in clusters. It also provides a physical explanation for the filamentary structures seen in optical emission-line observations of cluster cores (Conselice et al. 2001; Sparks et al. 2004). Note that simulations with isotropic conduction show no preference for the cold gas to align with the magnetic field direction (e.g., Figure 7).

The filamentary structure in the cold gas is also imprinted on the diffuse X-ray-emitting plasma in the hot ICM (e.g., Figure 4). Because of the large conductivity of the hot plasma (Equation (11)), it is natural for a given magnetic field line to become relatively isothermal. If different magnetic field lines undergo slightly different heating/cooling, as must surely be the case to some extent, this will lead to different temperatures, densities, and X-ray emissivities along different magnetic field lines. This could potentially explain the long, soft X-ray-emitting isothermal structures observed in some clusters (Sun et al. 2010).

The ambient cluster magnetic field is enhanced by flux freezing during the formation of filaments. Moreover, this enhancement of B extends over a region that is much longer than the extent of the cold gas itself (compare Figure 5 for $|B|$ with Figure 4 for T). This is because as the plasma compresses along the magnetic field, it leaves behind regions devoid of much cool plasma that have nonetheless had field amplification by flux freezing. The volume-averaged velocities induced by the thermal instability are ~ 25 km s $^{-1}$ for our typical cluster parameters. The velocity in the hot phase is, on average, directed toward the cold filaments; velocities in the cold filaments are larger (~ 100 km s $^{-1}$), are generally parallel to the filaments, and may have strong shear (because of the merger of oppositely moving filaments; see the right panel of Figure 5). The velocities ~ 100 km s $^{-1}$ we find in cold filaments are similar to the measured random velocities of optical emission-line filaments (e.g., Hatch et al. 2006). However, this comparison may be misleading because we ignore gravity in our simulations which can easily induce large motions in the dense filaments.

The length of cold filaments along the magnetic field roughly scales with the Field length in the cold phase. The width of filaments is also determined by the perpendicular Field length. For a realistic atomic cooling curve in which the cold atomic gas is at $\sim 10^4$ K, the filaments are expected to be extremely

small $\sim 10^{-4}$ pc. However, the observed atomic (e.g., H α) filaments are much longer than this. This can be explained if the filaments are supported by cosmic-ray (or some other form of isotropic non-thermal pressure, e.g., due to small-scale magnetic fields) pressure which prevents the collapse of the cold gas (see Figures 8 and 12). The presence of a significant population of cosmic rays is also inferred by modeling the atomic and molecular lines from clusters (Ferland et al. 2009). Even if the cosmic-ray pressure is small in the diffuse ICM ($p_{\text{cr}}/p \gtrsim 10^{-4}$), adiabatic compression will result in cosmic-ray-dominated cold filaments. For the scales of interest, cosmic-ray diffusion can be neglected if the cosmic-ray diffusion coefficient is equal to the Galactic value ($10^{28} \text{ cm}^2 \text{ s}^{-1}$; Berezhinskii et al. 1990); Sharma et al. (2009a) argue that this is likely to be the case. Other loss processes (e.g., pion production, ionization, Alfvén-wave excitation) may, however, be important, and could modify how effectively cosmic rays can support filaments (Section 4.4); this will be studied in more detail in future work. If cosmic-ray pressure is indeed substantial, the pressure of the thermal plasma in cold filaments can be significantly smaller than that of the ambient ICM. Substantial cosmic-ray (and magnetic) pressure could in principle help explain the lack of star formation in the molecular filaments of NGC 1275 (e.g., Fabian et al. 2008; Salomé et al. 2006). Hadronic interactions between cosmic rays and thermal nucleons in dense filaments can produce a significant gamma-ray flux due to neutral pion decay; however, because of the small volume occupied by the filaments, it is unlikely that the filaments will be detectable by current instruments. Simulations with gravity are required to assess whether non-thermal pressure support is truly required to obtain elongated filaments, or whether gravitational/tidal effects can produce them.

The perpendicular thickness of the filaments in our calculations is set largely by the isotropic diffusivity we include to ensure numerical convergence; in reality, however, the perpendicular thermal conductivity is negligible and some other physics (perhaps cosmic-ray pressure again) must determine the perpendicular scale of the filaments. The properties of observed filaments can in principle be tested by Faraday rotation measured along and across the filaments; the Faraday rotation should be substantial ($\sim 10^7 \text{ rad m}^{-2}$ for $n_e \sim 10 \text{ cm}^{-3}$, $B \sim 10 \mu\text{G}$, and a filament length of 10 kpc). However, these observations are difficult precisely because the filaments are narrow and because this requires a reasonably strong radio source behind the filament.

We have not included gravity in our simulations in order to focus on the thermal phase structure of the ICM and not the ICM dynamics. In stratified plasmas there will be a complex interplay between the thermal instability and buoyant motions (e.g., driven by buoyancy instabilities; see Parrish et al. 2009); this will be the focus of future work. In the nonlinear limit, cold, dense filaments are expected to fall, almost at the free fall rate, toward the cluster center. Magnetic anchoring and levitation by underdense, buoyant bubbles may, however, prevent this (e.g., Hatch et al. 2006; Revaz et al. 2008). Another important effect that we have ignored in present calculations is turbulence because of galaxy wakes or AGN jets. Turbulence will definitely affect the orientation of magnetic field lines, and hence determining the structure of the filaments. A detailed analysis of the effect of turbulence on thermal instability is beyond the scope of the present paper and will be addressed in future. Even with a significant gravitational field and turbulence, we expect the filaments to be aligned with the local magnetic

field as a consequence of the basic thermal physics of the ICM (i.e., cooling and anisotropic thermal conduction).

It is a pleasure to acknowledge useful discussions with Chris McKee, Jim Stone, and particularly Eve Ostriker. Support for P.S. and I.J.P. was provided by NASA through Chandra Postdoctoral Fellowship grant numbers PF8-90054 and PF7-80049 awarded by the Chandra X-ray Center, which is operated by the Smithsonian Astrophysical Observatory for NASA under contract NAS8-03060. E.Q. was supported in part by the David and Lucile Packard Foundation and NASA grant NNX10AC95G. We thank the Laboratory for Computational Astrophysics, University of California, San Diego, for developing ZEUS-MP and providing it to the community. This research was supported in part by the National Science Foundation through TeraGrid resources provided by NCSA and Purdue University. The simulations reported in the paper were carried out on the Abe cluster at NCSA and the Steele cluster at Purdue University.

APPENDIX

LINEAR STABILITY ANALYSIS

We assume a background hydrostatic and thermal equilibrium. Let the equilibrium quantities (ρ_0 , \mathbf{B}_0 , p_0 , $p_{\text{cr},0}$) be constant in space; the following analysis is valid for $kH \gg 1$ where k is the wavenumber and H is the scale over which equilibrium quantities vary. We do not include gravity in the following analysis, and hence because of $kH \gg 1$ all terms involving background gradients are small.

Perturbations of the form $e^{(-iwt+i\mathbf{k}\cdot\mathbf{x})}$ are assumed, where w is the frequency. Linear perturbations are preceded by a δ and equilibrium quantities have a subscript 0. The linearized equations are given by

$$\frac{\delta\rho}{\rho_0} + i\mathbf{k}\cdot\boldsymbol{\xi} = 0, \quad (\text{A1})$$

where $\boldsymbol{\xi} \equiv i\delta\mathbf{v}/\omega$ is the displacement vector,

$$-w^2\boldsymbol{\xi} = -i\mathbf{k}\frac{\delta(p + p_{\text{cr}} + B^2/8\pi)}{\rho_0} + \frac{i\mathbf{k}\cdot\mathbf{B}_0}{4\pi\rho_0}\delta\mathbf{B}, \quad (\text{A2})$$

$$\delta\mathbf{B} = i(\mathbf{k}\cdot\mathbf{B}_0)\boldsymbol{\xi} - i(\mathbf{k}\cdot\boldsymbol{\xi})\mathbf{B}_0, \quad (\text{A3})$$

$$-iw\frac{(\delta p - \gamma v_t^2 \delta\rho)}{\gamma - 1} = -\delta[n_e n_i \Lambda(T)] - i\mathbf{k}\cdot\boldsymbol{\delta Q}, \quad (\text{A4})$$

where $v_t^2 \equiv p/\rho$, and the perturbation of the spatially constant $H(t)$ vanishes as it equals the volume-averaged cooling rate which is constant in time in the linear regime,

$$-iw(\delta p_{\text{cr}} - \gamma_{\text{cr}} v_{t,\text{cr}}^2 \delta\rho) = -i\mathbf{k}\cdot\boldsymbol{\delta\Gamma}, \quad (\text{A5})$$

where $v_{t,\text{cr}}^2 \equiv p_{\text{cr}}/\rho$.

A.1. Fast Sonic Speed Limit

Dotting Equation (A2) with \mathbf{k} gives $\delta p_t/p_t \sim (t_{\text{snd}}/t_{\text{cool}})^2 \delta\rho/\rho_0$, where $p_t = p + p_{\text{cr}} + B^2/8\pi$, $t_{\text{snd}}^{-1} \sim k(p_t/\rho)^{1/2}$, and $w \sim t_{\text{cool}}^{-1}$ (i.e., we consider the condensation mode which grows at the cooling time; $t_{\text{cool}}^{-1} \equiv (\gamma - 1)n_e n_i \Lambda/p_0$). In the limit when the sound-crossing time is shorter than the cooling time, the relative perturbation in total pressure is much smaller

than the relative perturbation in density. Thus, we can combine Equations (A3)–(A5) to give

$$\begin{aligned} -iw\delta p_t = & -iw(\gamma v_t^2 + \gamma_{\text{cr}} v_{t,\text{cr}}^2) \delta\rho - iw\delta\left(\frac{B^2}{8\pi}\right) \\ & - (\gamma - 1)\delta[n_en_i\Lambda(T)] - (\gamma - 1)i\mathbf{k} \cdot \boldsymbol{\delta Q} - i\mathbf{k} \cdot \boldsymbol{\delta\Gamma}. \end{aligned} \quad (\text{A6})$$

Now in the limit of $t_{\text{snd}} \ll t_{\text{cool}}$, the left-hand side of Equation (A6) can be ignored with respect to the first term on the right-hand side. In this limit, from Equation (A3), we obtain

$$\delta(B^2/8\pi) = v_A^2 \delta\rho / (1 - k_{\parallel}^2 v_A^2/w^2), \quad (\text{A7})$$

where $v_A^2 \equiv B_0^2/4\pi\rho_0$ and $k_{\parallel} = \mathbf{k} \cdot \hat{\mathbf{b}}_0$. Thus in the short sound-crossing time limit, Equation (A6) reduces to

$$\begin{aligned} & iw\left(\gamma v_t^2 + \gamma_{\text{cr}} v_{t,\text{cr}}^2 + \frac{v_A^2}{1 - k_{\parallel}^2 v_A^2/w^2}\right) \delta\rho \\ & = -(\gamma - 1)\delta[n_en_i\Lambda(T)] - (\gamma - 1)i\mathbf{k} \cdot \boldsymbol{\delta Q} - i\mathbf{k} \cdot \boldsymbol{\delta\Gamma}, \end{aligned} \quad (\text{A8})$$

where p_t is held constant in evaluating the right-hand side. The cooling term can be written as

$$\begin{aligned} \delta[n_en_i\Lambda(T)]_{p_t} = & \frac{\partial[n_en_i\Lambda(T)]}{\partial\rho}|_p \delta\rho \\ & - \frac{\partial[n_en_i\Lambda(T)]}{\partial p}|_{\rho} \delta(p_{\text{cr}} + B^2/8\pi), \end{aligned} \quad (\text{A9})$$

where $\partial[n_en_i\Lambda(T)]/\partial p|_{\rho} = (n_en_i T/p)d\Lambda/dT$, and $\partial[n_en_i\Lambda(T)]/\partial\rho|_p = -(n_en_i T^3/\rho)d[\Lambda/T^2]/dT$. Thus, Equation (A9), on combining with Equation (A7), becomes

$$\begin{aligned} \delta \ln[n_en_i\Lambda(T)]_{p_t} = & -\frac{d \ln \Lambda}{d \ln T} \frac{\delta p_{\text{cr}}}{p_0} - \left[\frac{d \ln(\Lambda/T^2)}{d \ln T} \right. \\ & \left. + \frac{2}{\beta(1 - k_{\parallel}^2 v_A^2/w^2)} \frac{d \ln \Lambda}{d \ln T} \right] \frac{\delta\rho}{\rho_0}, \end{aligned} \quad (\text{A10})$$

where $\beta \equiv 8\pi p/B^2$. From Equation (7) we obtain $i\mathbf{k} \cdot \boldsymbol{\delta\Gamma} = D_{\parallel} k_{\parallel}^2 \delta p_{\text{cr}}$, so combining with Equation (A5), we obtain

$$\delta p_{\text{cr}} = \frac{-iw\gamma_{\text{cr}} v_{t,\text{cr}}^2 \delta\rho}{(-iw + D_{\parallel} k_{\parallel}^2)}. \quad (\text{A11})$$

Similarly, $i\mathbf{k} \cdot \boldsymbol{\delta Q} = \kappa k_{\parallel}^2 \delta T$, and on using Equations (A4) and (A10), gives

$$\begin{aligned} (-iw + \chi_{\parallel} k_{\parallel}^2) \frac{\delta p}{p_0} = & t_{\text{cool}}^{-1} \frac{d \ln \Lambda}{d \ln T} \frac{\delta p_{\text{cr}}}{p_0} + \left(-iw\gamma + \chi_{\parallel} k_{\parallel}^2 + t_{\text{cool}}^{-1} \right. \\ & \times \left. \left[\frac{d \ln(\Lambda/T^2)}{d \ln T} + \frac{2}{\beta(1 - k_{\parallel}^2 v_A^2/w^2)} \frac{d \ln \Lambda}{d \ln T} \right] \right) \frac{\delta\rho}{\rho_0}, \end{aligned} \quad (\text{A12})$$

where $\chi_{\parallel} \equiv (\gamma - 1)\kappa_{\parallel} T/p$ is the thermal diffusivity. Combining Equations (A12), (A11), and (A7), and using $\delta p_t \approx 0$ gives

$$\begin{aligned} & \frac{-iw\alpha}{(-iw + D_{\parallel} k_{\parallel}^2)} \left(-iw + \chi_{\parallel} k_{\parallel}^2 + t_{\text{cool}}^{-1} \frac{d \ln \Lambda}{d \ln T} \right) - \frac{2}{\beta} \frac{(-iw + \chi_{\parallel} k_{\parallel}^2)}{(1 - k_{\parallel}^2 v_A^2/w^2)} \\ & = -iw\gamma + \chi_{\parallel} k_{\parallel}^2 + t_{\text{cool}}^{-1} \left[\frac{d \ln(\Lambda/T^2)}{d \ln T} + \frac{2}{\beta(1 - k_{\parallel}^2 v_A^2/w^2)} \frac{d \ln \Lambda}{d \ln T} \right], \end{aligned} \quad (\text{A13})$$

where $\alpha = p_{\text{cr}}/p$. In the hydro limit ($\alpha \ll 1$ and $\beta \gg 1$, irrespective of $k_{\parallel}^2 v_A^2 t_{\text{cool}}^{-2}$; i.e., magnetic tension plays no role in the condensation mode), we recover the classic isobaric thermal instability stabilized by conduction along field lines (Equation (8)). For $\beta \ll 1$ or $\alpha \gg 1$ one obtains the thermal instability in the isochoric limit (see the next section), with conductive stabilization for scales smaller than the isochoric Field length (Equation (10)). The condensation mode is isochoric when magnetic/cosmic-ray pressure dominates because the constancy of the total pressure is equivalent to the constancy of the magnetic/cosmic-ray pressure, and from Equations (A7) and (A11) a constant magnetic/cosmic-ray pressure implies a constant density.

A.2. Slow Sonic Speed Limit

In the opposite limit, $t_{\text{cool}} \ll t_{\text{snd}}$, $\delta\rho/\rho \ll \delta p_t/p_t$, Equation (A6) gives

$$-iw\delta p_t = -(\gamma - 1)\delta[n_en_i\Lambda(T)] - (\gamma - 1)i\mathbf{k} \cdot \boldsymbol{\delta Q} - i\mathbf{k} \cdot \boldsymbol{\delta\Gamma}, \quad (\text{A14})$$

where the terms on the right-hand side are evaluated keeping the density constant (i.e., isochoric). The perturbed magnetic and cosmic-ray pressures vanish in the isochoric limit (Equations (A7) and (A11)) and $\delta p_t = \delta p$, and the dispersion relation is the same as Equation (10).

REFERENCES

- Audit, E., & Hennebelle, P. 2005, *A&A*, **433**, 1
- Balbus, S. A. 2000, *ApJ*, **534**, 420
- Balbus, S. A., & Soker, N. 1989, *ApJ*, **341**, 611
- Berezinskii, V. S., Bulanov, S. V., Dogiel, V. A., & Ptuskin, V. S. 1990, in *Astrophysics of Cosmic Rays*, ed. V. L. Ginzburg (Amsterdam: North-Holland)
- Braginskii, S. I. 1965, in *Reviews of Plasma Physics*, Vol. 1, ed. M. A. Leontovich (New York: Consultants Bureau), 205
- Cavagnolo, K. W., Donahue, M., Voil, G. M., & Sun, M. 2008, *ApJ*, **683**, L107
- Conselice, C. J., Gallagher, J. S., & Wyse, R. F. G., III 2001, *AJ*, **122**, 2281
- Fabian, A. C. 1994, *ARA&A*, **32**, 277
- Fabian, A. C., Johnstone, R. M., Sanders, J. S., Conselice, C. J., Crawford, C. S., Gallagher, J. S., & Zweibel, E. 2008, *Nature*, **454**, 968
- Ferland, G. J., Fabian, A. C., Hatch, N. A., Johnstone, R. M., Porter, R. L., van Hoof, P. A. M., & Williams, R. J. R. 2009, *MNRAS*, **392**, 1475
- Field, G. B. 1965, *ApJ*, **142**, 531
- Guo, F., & Oh, S. P. 2008, *MNRAS*, **384**, 251
- Guo, F., Oh, S. P., & Ruszkowski, M. 2008, *ApJ*, **688**, 859
- Hatch, N. A., Crawford, C. S., Johnstone, R. M., & Fabian, A. C. 2006, *MNRAS*, **367**, 433
- Hayes, J., et al. 2006, *ApJ*, **165**, 188
- Karpen, J. T., Picone, J. M., & Dahlburg, R. B. 1988, *ApJ*, **324**, 590
- Koyama, H., & Inutsuka, S. 2000, *ApJ*, **532**, 980
- Koyama, H., & Inutsuka, S. 2004, *ApJ*, **602**, 25
- Kritsuk, A. G., & Norman, M. L. 2002, *ApJ*, **569**, L127
- Kunz, M. W., Schekochihin, A. A., Cowley, S. C., Binney, J. J., & Sanders, J. S. 2010, arXiv:1003.2719
- Loewenstein, M., Zweibel, E. G., & Begelman, M. C. 1991, *ApJ*, **377**, 392
- McKee, C. F., & Ostriker, J. P. 1977, *ApJ*, **218**, 148
- O'Dea, C. P., et al. 2008, *ApJ*, **681**, 1035
- Parrish, I. J., Quataert, E., & Sharma, P. 2009, *ApJ*, **703**, 96
- Parrish, I. J., Quataert, E., & Sharma, P. 2010, *ApJ*, **712**, L194
- Peterson, J. R., et al. 2003, *ApJ*, **590**, 207
- Piontek, R. A., & Ostriker, E. C. 2004, *ApJ*, **601**, 905
- Quataert, E. 2008, *ApJ*, **673**, 758
- Revaz, Y., Combes, F., & Salomé, 2008, *A&A*, **477**, L33
- Salomé, P., et al. 2006, *A&A*, **454**, 437
- Sánchez-Salcedo, F. J., Vázquez-Semadeni, E., & Gazol, A. 2002, *ApJ*, **577**, 768
- Schlickeiser, R. 2002, in *Cosmic Ray Astrophysics*, (Berlin: Springer)

- Sharma, P., Chandran, B. D. G., Quataert, E., & Parrish, I. J. 2009a, *ApJ*, **699**, 348
- Sharma, P., Chandran, B. D. G., Quataert, E., & Parrish, I. J. 2009b, in AIP Conf. Proc. 1201, The Monster's Fiery Breath: Feedback in Galaxies, Groups, & Clusters, ed. S. Heinz & E. Wilcots (Melville, NY: AIP), 363
- Sharma, P., Colella, P., & Martin, D. F. 2009c, SIAM J. Sci. Comput., submitted (arXiv:0909.5426)
- Sharma, P., & Hammett, G. W. 2007, *J. Comput. Phys.*, **227**, 123
- Sparks, W. B., Donahue, M., Jordán, A., Ferrarese, L., & Côté, 2004, *ApJ*, **607**, 294
- Sun, M., Donahue, M., Roediger, E., Nulsen, P. E. J., Voit, G. M., Sarazin, C., Forman, W., & Jones, C. 2010, *ApJ*, **708**, 946
- Sutherland, R. S., & Dopita, M. A. 1993, *ApJS*, **88**, 253
- Tozzi, P., & Norman, C. 2001, *ApJ*, **546**, 63